International Journal of Heat and Mass Transfer 52 (2009) 636–643

Contents lists available at ScienceDirect

International Journal of Heat and Mass Transfer

journal homepage: www.elsevier.com/locate/ijhmt

Study on flow and heat transfer characteristics of heat pipe with axial "Ω"-shaped microgrooves

Yongping Chen [a,*], Chengbin Zhang [a], Mingheng Shi [a], Jiafeng Wu [a], G.P. Peterson [b]

[a] School of Energy and Environment, Southeast University, Nanjing, Jiangsu 210096, PR China
[b] Office of the Chancellor, University of Colorado at Boulder, Regent Administrative Center, 17 UCB, 2 Boulder, CO 80309-001, USA

ARTICLE INFO

Article history:
Received 14 March 2008
Received in revised form 31 July 2008
Available online 7 October 2008

Keywords:
Heat pipe
Microgrooves
Capillary radius
Maximum heat transport capability

ABSTRACT

A theoretical model of fluid flow and heat transfer in a heat pipe with axial "Ω"-shaped grooves has been conducted to study the maximum heat transport capability of these types of heat pipes. The influence of variations in the capillary radius, liquid–vapor interfacial shear stress and the contact angle are all considered and analyzed. The effect of vapor core and wick structure on the fluid flow characteristics and the effect of the heat load on the capillary radius at the evaporator end cap, as well as the effect of the wick structure on the heat transfer performance are all analyzed numerically and discussed. The axial distribution of the capillary radius, fluid pressure and mean velocity are obtained. In addition, the calculated maximum heat transport capability of the heat pipe at different working temperatures is compared with that obtained from a traditional capillary pressure balance model, in which the interfacial shear stress is neglected. The accuracy of the present model is verified by experimental data obtained in this paper.

1. Introduction

Heat pipes with axial "Ω"-shaped microgrooves (see Fig. 1) have been introduced as an attractive option for a wide variety of advanced thermal devices, such as spacecraft thermal control systems and microelectronic cooling systems, due to the powerful heat transfer capability, stable operation under microgravity conditions and the high degree of temperature uniformity [1,2].

The heat pipe with microgrooves is charged with the appropriate amount of working fluid. The heat flux is applied to the evaporator section, where to vaporize the liquid. The vapor condenses at the condenser section to release the latent heat. The condensate will be driven from the condenser back to the evaporator by the capillary pressure created in the microgrooves [3–5].

There have been a few investigations on heat pipe with microgrooves wick structure [6–18], especially in the design, fabrication, and performance prediction. Benson [6–9], Kalahasti [10] at Sandia National Laboratory have been involved in the design and fabrication of a new kind of flat micro heat pipe spreaders with mushroom wick structure as passive heat dissipation devices. These microscale flat plate heat spreaders allow the heat to be dissipated in any direction across the wafer surface, and provide tremendous potential in dissipating heat from hot spots. These flat plate heat pipes have been found to be promising for situations where space available for the cooling system is a major constraint, such as in processor cooling in laptop computers, cooling of the solar energy collector panels in satellites, etc.

Differing from microscale flat plate heat pipe, heat pipes with axial microgrooves have been introduced as an attractive option for a wide variety of advanced thermal devices to transport heat in the long distance, such as spacecraft thermal control systems. These devices own the advantage of powerful heat transfer capability and the high effective thermal conductivity. Especially, as an optimum choice of high capacity grooved heat pipe in the frame provided by ESA (European Space Agency) [11], heat pipe with axial "Ω"-shaped microgrooves combines a high capillary pumping pressure with a low axial pressure drop in the liquid. Meanwhile, the retardation of the liquid flow due to the countercurrent vapor flow over the liquid–vapor interface is minimized as compared to other axial groove designs. In addition, entrainment limit is enhanced due to longer wet perimeter of wick groove and narrower slot width. However, compared with rectangular, trapezoidal, or triangular groove designs, the radial thermal resistance of "Ω"-shaped groove geometry may be larger and the boiling limit might be weakened due to an increase in the wall thickness of the heat pipe.

While there have been a majority of the available investigations on axially grooved heat pipe based on triangular [12,13], rectangular [14,15], or trapezoidal [16–18] grooves, especially in the prediction of the heat transport capability considering countercurrent vapor flow in open capillary grooves, there is relatively little work on "Ω"-shaped grooves in the literature. Thomas and Damle [1] proposed a good analysis on the fully developed laminar flow within a reentrant groove using a finite element model, and the

* Corresponding author. Tel.: +86 25 8379 3092.
E-mail address: ypchen@seu.edu.cn (Y. Chen).

0017-9310/$ - see front matter © 2008 Elsevier Ltd. All rights reserved.
doi:10.1016/j.ijheatmasstransfer.2008.08.003

Nomenclature

A	cross-sectional area, m^2
b_j	constant values, in Eq. (7)
A^*	dimensionless area, A/h^2
C_1	$\frac{1}{\mu}\frac{dP}{dz}$
D	hydraulic diameter, $4A/p$, m
D^*	dimensionless hydraulic diameter, D/h
d	diameter of wick structure (see Fig. 1), m
d_o	outer diameter of heat pipe, mm
f	friction coefficient
h	wall thickness of heat pipe, m
h_{fg}	latent heat, J/kg
$\dot{m}$	mass flow rate
L_a	adiabatic length, m
L_e	evaporator length, m
L_c	condenser length, m
N	number of grooves
n^*	dimensionless unit vector normal to meniscus, n/h
P	pressure, Pa
p	wetted perimeter, m
Po	Poiseuille number, $Po = fRe$
Q_{in}	input heat load, W
r_c	capillary radius, m
$r_{c,eva}$	capillary radius at evaporator section end cap, m
$r_{c,con}$	capillary radius at condenser section end cap, m
Re	Reynolds number
T	temperature, °C
w	velocity, m/s
$\bar{w}$	dimensionless velocity
$\overline{w^*}$	mean dimensionless velocity
w^*	dimensionless velocity
W	groove width (see Fig. 1), m
x^*, y^*	dimensionless coordinate
z	axial coordinate, m

Greek symbols

μ	dynamic viscosity, Pa.s
ρ	density, kg/m^3
θ	contact angle, rad
δ	slot height (see Fig. 1), mm
σ	surface tension coefficient, N/m
α	corner angel, rad
ϕ	the angle between n^* and x^*

Subscripts

l	liquid
v	vapor
lv	liquid–vapor interface
e	evaporator section
a	adiabatic section
c	condenser section

capillary limit of a low-temperature heat pipe was also determined based on traditional capillary pressure balance. However, Thomas' model only discussed the liquid flow in one reentrant groove cross-section, the axial distribution of fluid flow for both liquid and vapor and heat transfer in heat pipe, what is more important, has not been included. Therefore, in the current investigation, a model that couples the liquid and vapor flow in "Ω"-shaped microgrooves is developed on the basis of the analysis on the flow in the duct of arbitrary shape, suggested by Sparrow [19]. And a theoretical study of the performance of this advanced heat pipe is performed by analyzing the axial distribution of the capillary meniscus radius. In addition, a series of factors that influence the flow and heat transfer characteristics of the heat pipe with axial "Ω"-shaped grooves are analyzed and discussed. The accuracy of the present model is verified by experimental data obtained in this paper.

2. Theoretical model

2.1. Fluid flow

Some simplifying assumptions are required before deriving the governing equations. The major assumptions are:

(a) Steady fluid flow and heat transfer,
(b) Laminar flow,
(c) Constant fluid properties.

In axially grooved heat pipes, the liquid flows in the capillary microgrooves and vapor flows in the vapor core in a countercurrent fashion. For fully developed laminar flow with no body forces, the governing differential equations of the velocity distribution for both the vapor and liquid can be derived in the same format as [20]

$$\frac{\partial^2 w}{\partial x^2} + \frac{\partial^2 w}{\partial y^2} = \frac{1}{\mu}\frac{dP}{dz} \quad (1)$$

The dimensionless coordinates and velocity can be expressed as follows:

$$x^* = \frac{x}{h}, \quad y^* = \frac{y}{h}, \quad w^* = -\frac{w}{h^2 C_1} \quad (2)$$

where h is the wall thickness of heat pipe, $C_1 = \frac{1}{\mu}\frac{dP}{dz}$.

The non-dimensional form of Eq. (1) is

$$\frac{\partial^2 w^*}{\partial x^{*2}} + \frac{\partial^2 w^*}{\partial y^{*2}} = -1 \quad (3)$$

In order to reduce Eq. (3) to Laplace's equation, applying the following transformation:

$$w^* = w' - \frac{1}{4}(x^{*2} + y^{*2}) \quad (4)$$

Yield

$$\frac{\partial^2 w'}{\partial x^{*2}} + \frac{\partial^2 w'}{\partial y^{*2}} = 0 \quad (5)$$

For Laplace's equation, Eq. (5), the exact solution is as the following:

$$w' = \sum_{j=1}^{\infty} b_j g_j(x^*, y^*) \quad (6)$$

Combining Eqs. (3), (4), and (6), we have

$$w^* = \sum_{j=1}^{\infty} b_j g_j(x^*, y^*) - \frac{1}{4}(x^{*2} + y^{*2}) \quad (7)$$

where

$$g_j(x^*, y^*) = \begin{cases} \text{real parts of complex variable } (x^* + y^* i)^k, & j = 2k+1, \quad k = 0,1,2,3\ldots \\ \text{imaginary parts of complex variable } (x^* + y^* i)^k, & j = 2(k+1), \quad k = 0,1,2,3\ldots, \end{cases}$$

b_j are constant values determined by boundary conditions. In the numerical calculation, the first 42 terms of infinite series are

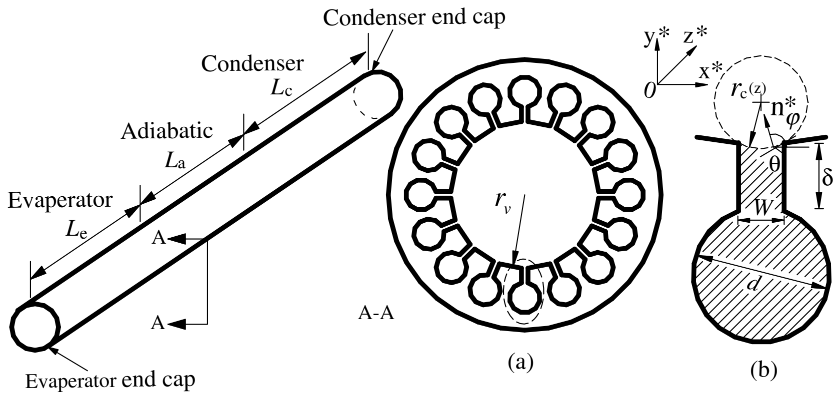

Fig. 1. Schematic of heat pipe with axial "Ω"-shaped grooves. (a) Cross-section (no interconnection among microgrooves at both ends). (b) Geometric shape of a "Ω"-shaped groove.

adopted to ensure the accuracy [19], so the number of series terms $m = 42$.

The differential Eq. (7) becomes

$$\frac{\partial w^*}{\partial n^*} = \frac{\partial w^*}{\partial x^*}\cos\varphi + \frac{\partial w^*}{\partial y^*}\sin\varphi = -\frac{x^*\cos\varphi + y^*\sin\varphi}{2} + \sum_{j=1}^{m} b_j\left(\frac{\partial g_j}{\partial x^*}\cos\varphi + \frac{\partial g_j}{\partial y^*}\sin\varphi\right) \tag{8}$$

where ϕ is the angle between n^* and x^*.

To simulate liquid flow at any point $(x^*_{\mathrm{w}}, y^*_{\mathrm{w}})$ on the wall, the no-slid condition ($w_{\mathrm{w}} = 0$) is applied. According to Eq. (7), the no-slid boundary condition can be written as

$$\frac{1}{4}(x^{*2}_{\mathrm{w}} + y^{*2}_{\mathrm{w}}) = \sum_{j=1}^{m} b_j g_j(x^*_{\mathrm{w}}, y^*_{\mathrm{w}}) \tag{9}$$

In axially grooved heat pipes, the average liquid velocity is much smaller than the average vapor velocity. Hence, the vapor velocity at any point $(x^*_{\mathrm{lv}}, y^*_{\mathrm{lv}})$ of the liquid–vapor interface is equal to the liquid velocity, thus it can be assumed to be zero ($w_{\mathrm{v}} = 0$) [15,21]. According to Eq. (7)

$$\frac{1}{4}(x^{*2}_{\mathrm{lv}} + y^{*2}_{\mathrm{lv}}) = \sum_{j=1}^{m} b_j g_j(x^*_{\mathrm{lv}}, y^*_{\mathrm{lv}}) \tag{10}$$

However, it must be accented that Eq. (10) is only employed in the calculation for the vapor flow.

The shape of the liquid–vapor interface can be assumed to be circular, and the shear stress on the liquid–vapor interface along the z direction is

$$\tau^*_{\mathrm{lv}} = \left.\frac{\partial w^*}{\partial n^*}\right|_{\mathrm{lv}} = \frac{\tau_{\mathrm{lv}}}{h(-\mathrm{d}P/\mathrm{d}z)} \tag{11}$$

where n^* is the coordinate normal to the liquid–vapor interface, and the shear force τ_{lv} on the liquid–vapor interface can be calculated as [20]

$$\tau_{\mathrm{lv}} = -f_{\mathrm{v}}\frac{\rho_{\mathrm{v}}\bar{w}^2_{\mathrm{v}}}{2} = -\frac{(fRe)_{\mathrm{v}}}{2D_{\mathrm{v}}}\mu_{\mathrm{v}}\bar{w}_{\mathrm{v}} \tag{12}$$

Combining Eqs. (12) and (11), the boundary condition at the liquid–vapor interface becomes

$$\left.\frac{\partial w^*_{\mathrm{l}}}{\partial n^*}\right|_{\mathrm{lv}} = -\frac{\mu_{\mathrm{v}}}{\mu_{\mathrm{l}}}\left.\frac{\partial w^*_{\mathrm{v}}}{\partial n^*}\right|_{\mathrm{lv}} = \frac{\mu_{\mathrm{v}}}{\mu_{\mathrm{l}}}\frac{(fRe)_{\mathrm{v}}}{2D^*_{\mathrm{v}}}\overline{w^*_{\mathrm{v}}} \tag{13}$$

where fRe is defined as the Poiseuille number.

Eq. (13) represents the principle of coupled liquid and vapor flow at the liquid–vapor interface in an axially grooved heat pipe, and this equation is only used to calculate the liquid velocity in grooved structure.

For vapor flow, according to Eqs. (9) and (10), $N(N > m)$ points on the liquid–vapor interface and wall to generate the over-determined matrix equations which consists of N equations and m unknown coefficients b_j in Eq. (7) are selected by using Householder method [22] to solve the over-determined matrix equations.

For liquid flow, according to Eqs. (8), (9) and (13), the coefficients b_j are determined by the same method. Therefore, the Poiseuille numbers for both vapor and liquid flow can be obtained from the numerical solution of velocity distribution in vapor core and groove using the following definition [19]

$$Po = fRe = \frac{D^{*2}}{2\overline{w^*}} \tag{14}$$

where the mean dimensionless velocity $\overline{w^*} = \frac{1}{A^*}\int\int_{A^*} w^*\mathrm{d}x^*\,\mathrm{d}y^*$, in which the dimensionless area $A^* = A/h^2$, dimensionless hydraulic diameter $D^* = 4A/(hp)$, p is the wetted perimeter.

2.2. Maximum heat transport capability

For any location, z, along the axial length of heat pipe as shown in Fig. 1(b), the capillary pressure P_{c} can be calculated by the Laplace–Young equation [23]

$$P_{\mathrm{c}} = P_{\mathrm{v}} - P_{\mathrm{l}} = \sigma\left(\frac{1}{r_{\mathrm{c1}}} + \frac{1}{r_{\mathrm{c2}}}\right) \tag{15}$$

where r_{c1} and r_{c2} are the radial and axial capillary radius of the meniscus, respectively. Since $r_{\mathrm{c2}} \gg r_{\mathrm{c1}}$, it is quite reasonable to assume that $r_{\mathrm{c2}} \to \infty$ and $r_{\mathrm{c1}} \approx r_{\mathrm{c}}(z)$. The differential form of Eq. (15) becomes

$$\frac{\mathrm{d}P_{\mathrm{v}}}{\mathrm{d}z} - \frac{\mathrm{d}P_{\mathrm{l}}}{\mathrm{d}z} = -\frac{\sigma}{r^2_{\mathrm{c}}(z)}\frac{\mathrm{d}r_{\mathrm{c}}(z)}{\mathrm{d}z} \tag{16}$$

For laminar flow, both the vapor and liquid pressure distribution along the stream can be determined from

$$\frac{\mathrm{d}P}{\mathrm{d}z} = -f\frac{2\rho\bar{w}^2}{D} = -\frac{2\mu(fRe)\bar{w}}{D^2} \tag{17}$$

The mean velocity can be calculated as

$$\bar{w} = \frac{\dot{m}(z)}{A\rho} \tag{18}$$

where $\dot{m}(z)$ is the mass flow rate at location z.

Substituting Eq. (18) into Eq. (17)

$$\frac{dP}{dz} = -\frac{2\mu(fRe)\dot{m}(z)}{\rho A D^2} \tag{19}$$

In order to simplify the calculation, it is reasonable to assume that the length of liquid block [24] formed at the condenser section end cap due to slight overcharging of the working fluid can be neglected and the evaporator and condenser sections are under the constant heat flux boundary condition. Therefore, the mass flow rate can be obtained by the energy conservation equation

$$\dot{m}_v(z) = -\dot{m}_l(z) = \frac{Q(z)}{h_{fg}} \tag{20}$$

The axial heat flux, $Q(z)$, is specified as

$$Q(z) = \begin{cases} \frac{z}{L_e} Q_{in}, & 0 \leqslant z \leqslant L_e \\ Q_{in}, & L_e < z < L_e + L_a \\ \frac{L_e + L_a + L_c - z}{L_c} Q_{in}, & L_e + L_a \leqslant z \leqslant L_e + L_a + L_c \end{cases} \tag{21}$$

where L is the length of heat pipe, Q_{in} is the input heat load.

Combining Eqs. (15), (16), (19), (20) and (21) yields an ordinary differential equation for $r_c(z)$ as

$$\frac{dr_c(z)}{dz} = f(z, r_c(z), Q_{in}, T_{work}, \text{geometry}) \tag{22}$$

Once the radius at the condenser section end cap $r_{c,con}(z = L_e + L_a + L_c)$ is determined for the given heat load Q_{in}, heat pipe geometry and working temperature, the capillary meniscus radius at any location z along the axial can be solved numerically using the fourth-order Runge–Kutta method. At the point of condenser section end cap ($z = L_e + L_a + L_c$), the vapor and liquid pressure can be expressed as

$$P_v = P_{v0}, \quad P_l = P_{v0} - \frac{\sigma}{r_{c,con}} (z = L_e + L_a + L_c) \tag{23}$$

where P_{v0} is the vapor pressure at the condenser section end cap, $r_{c,con} = r_v$ [25,26], in which r_v is the radius of the vapor core.

On the basis of the analysis of capillary flow in the microgroove [26], when the heat pipe with axial "Ω"-shaped microgrooves works in steady-state and reaches the maximum heat transport capability, the capillary radius at the evaporator section end cap ($z = 0$) can be expressed as $r_{c,eva} = W/(2\cos\theta)$, in which θ is the contact angle. Therefore, the maximum heat transport capability can be predicted on the basis of the analysis of the axial distribution of the capillary meniscus radius. The calculation procedure can be summarized as follows:

(1) Assume an initial value of heat load Q_{in}.
(2) Determine $r_c(z)$ at $z = 0$ by solving Eq. (22).
(3) If $r_c(0) > r_{c,eva}$, choose a larger value of Q_{in} and recalculate $r_c(0)$, else, choose a smaller Q_{in} and recalculate $r_c(0)$.
(4) Repeat step (2), (3) until $|r_c(0) - r_{c,eva}|$ reaches the convergence condition, and then regard Q_{in} as the maximum heat transport capability Q_{max}.

3. Results and discussion

3.1. Analysis of flow characteristics

For countercurrent vapor and liquid flow in an axially heat pipe with a grooved wick, the shear force on vapor–liquid interface depends upon $(Po)_v$. As shown in Fig. 2, with a small contact angle, $(Po)_v$ varies with the heat pipe geometry. However, when the contact angle is larger than 60°, despite the different geometry, it is approximately constant. The Poiseuille number for the liquid flow

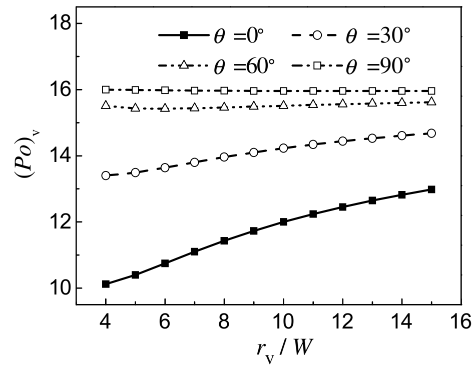

Fig. 2. $(Po)_v$ versus vapor core structure.

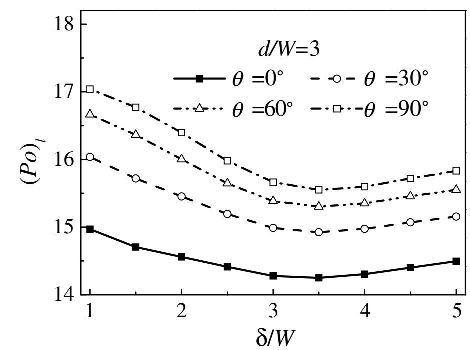

Fig. 3. $(Po)_l$ versus slot height ($\tau^*_{lv} = 1$).

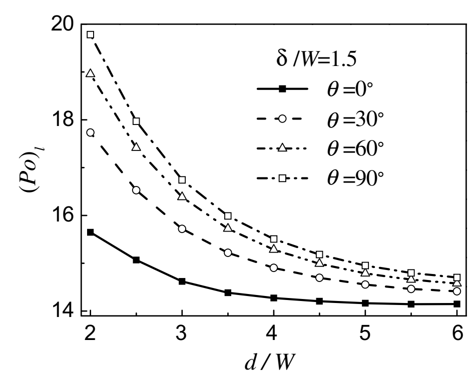

Fig. 4. $(Po)_l$ versus wick diameter ($\tau^*_{lv} = 1$).

is given in Figs. 3 and 4 as a function of the groove geometry with different wetting angles, θ. The working fluid flow is deeply influenced by $(Po)_l$.

The capillary meniscus radius at the evaporator section end cap depends on the groove configuration, contact angle, and heat load. For a given grooved heat pipe (see Table 1), the groove geometry is known, the meniscus radius will only depend upon the heat load. Fig. 5 illustrates the effect of the heat load on the capillary radius at the evaporator section end cap ($z = 0$). As shown in the figure, the meniscus radius at the evaporator section end cap decreases with the increase of the heat load. The decrease in this meniscus radius which influences the capillary radius distribution results in a much thinner evaporating liquid film at the evaporator section. Therefore, the capillary pumping ability and the heat transport capability would also increase. And the heat pipe reaches the maximum heat transport capability when the minimal meniscus radius at the evaporator section end cap is obtained.

Table 1
Specification of heat pipe with axial "Ω"-shaped grooves

Number of groove N	Outside diameter d_o (mm)	Vapor core radius r_v (mm)	Wick diameter D (mm)	Wick slot height δ (mm)
16	4.5	1.40	0.36	0.18
Wick slot width W (mm) 0.12	Evaporator length L_e (cm) 10	Condenser length L_c (cm) 10	Adiabatic length L_a (cm) 8.5	Contact angle θ (°) 45.6
Working temperature T_{work} (K) 293	Working fluid Ammonia	Solid material Aluminum alloy		

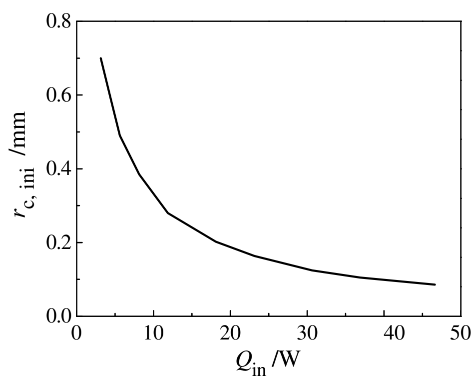

Fig. 5. Capillary radius at evaporator end cap versus heat load.

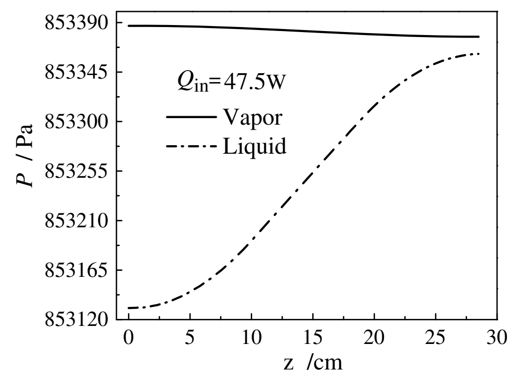

Fig. 7. Axial distribution of liquid and vapor pressure.

Fig. 6 represents the distribution of capillary radius along the axial direction for the given grooved heat pipe. As shown in this figure, the capillary radius increases slowly and non-linearly along the axial direction at the evaporator and adiabatic section, while it begins to increase drastically at the beginning of the condenser section.

Fig. 7 illustrates the pressure distributions for both vapor and liquid. Because the pressure difference between the liquid and the vapor is inversely proportional to the capillary radius, at the evaporator and adiabatic section this pressure difference is much larger, while what in condenser section is smaller. As shown in this figure, with the increase of the capillary radius along the axis, the pressure in liquid would increase along the axial direction, and the narrow slot of the "Ω"-shaped groove weakens the shear force of vapor on liquid, thus the condensate would be driven from the condenser back to the evaporator easily by the capillary force. And it is also indicated by the figure that the variation of liquid pressure along the stream is much lager than what in vapor.

The variations of the mean axial velocity of the liquid and vapor are shown in Fig. 8. The velocities of both liquid and vapor are zero at two ends of heat pipe. The axial velocity of the vapor in the evaporator region increases linearly along z direction due to continuous evaporation of liquid by the heat load, while that in the condenser region decreases linearly owing to the condensation of vapor by the heat remove. The condensate flow direction, which is from the condenser end cap back to the evaporator end cap, is inverse to the vapor flow direction. And the condensate velocity increases linearly along the liquid stream at the condenser section and decreases at the evaporator section. In the adiabatic region, the axial velocities for both liquid and vapor almost keep in constant due to no phase change occur.

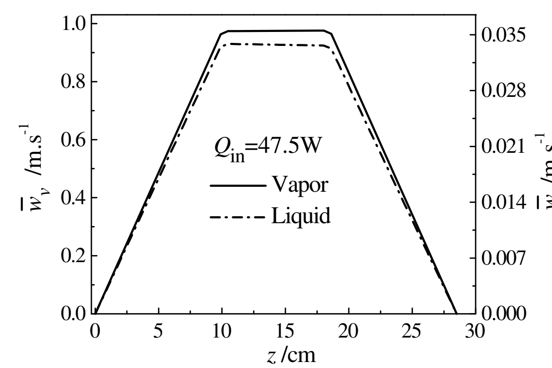

Fig. 8. Axial distribution of velocity for vapor and liquid.

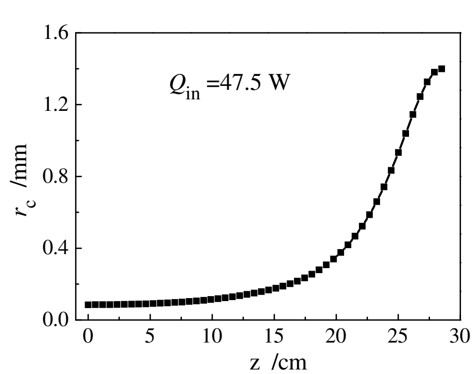

Fig. 6. Axial distribution of capillary radius.

3.2. Analysis of maximum heat transport capability

Fig. 9 shows the maximum heat transport capability of grooved heat pipe with respect to the operation temperature, in which the present result is plotted in the solid line and what from Chi [27] is plotted in the dash dotted line. As shown in Fig. 9, for the case studied in this work, the peak point of the maximum heat transport capability appears at 265 K, and the heat transfer performance

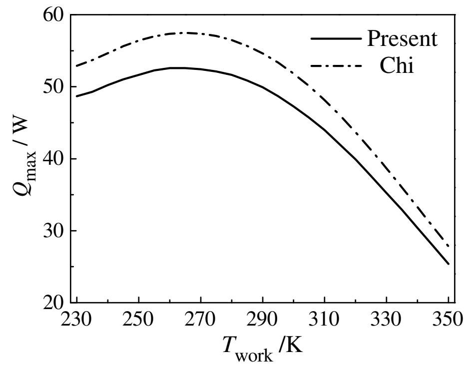

Fig. 9. Variation of Q_{max} at different working temperature.

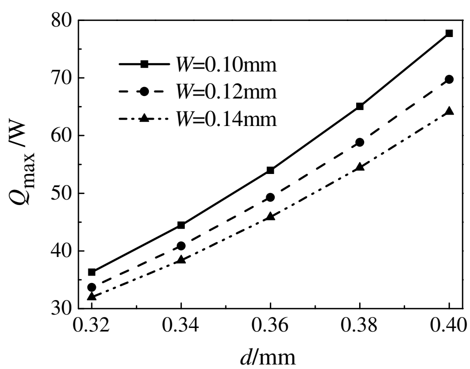

Fig. 10. Q_{max} versus wick size.

is good at 230–300 K while it is deteriorated at the high temperature. The maximum heat transport capability predicted by the present model is lower than what from Chi [27], which is due to the effects of the liquid–vapor interfacial shear stress and variation of meniscus radius that had not been considered in Chi's model [27].

Fig. 10 presents the maximum heat transport capability versus wick diameter and slot width. As shown in the figure, for the heat pipe (see Table 1), the maximum heat transport capability increases with the increase of wick diameter or the decrease of wick slot width since the narrower wick slot can produce higher capillary pumping pressure, and the increase of wick diameter makes the permeability to be stronger. However, smaller wick slot width might also increase friction loss, and larger wick diameter would also decrease effective thermal conductivity of wick structure layer. Therefore, based on the mechanical manufacture capacity, optimization design of the "Ω"-shaped wick geometry for both flow and thermal considerations is very important for engineering application.

4. Experimental verification

In order to verify the present mathematical model, an experiment of the maximum heat transport capability of a "Ω"-shaped heat pipe with the geometry shown in Fig. 11 is conducted. As shown in Fig. 12, the evaporator section is heated by the heater tape (OMEGA FGS101-060), and the condenser section is cooled by cooling water with constant temperature. The axial temperature distribution of the heat pipe is measured by thermocouple, and the working temperature is regarded as the mean value of these measured temperatures.

When the input heat load reached a value Q_{in}, if a smaller heat load increase, ΔQ_{in}, will make the temperature of evaporator end cap increased drastically, this value Q_{in}, will be determined as the maximum heat transport capability Q_{max}. This phenomenon of temperature drastic increase indicates that the evaporator section is partially dried out due to over evaporation and no sufficient capillary force to pump back the condensate. In such case, the thermal performance of the heat pipe would be deteriorated. The drastic increase of temperature at evaporator end cap also implies that capillary limit is a constraint for heat transfer, but not any other kind of operation limitation, such as instability owing to upstream compressible volume [28–31].

Table 2 is the comparison between the experimental data with the calculated results from the present model. It can be seen the largest error of maximum heat transport capability is 14%. The

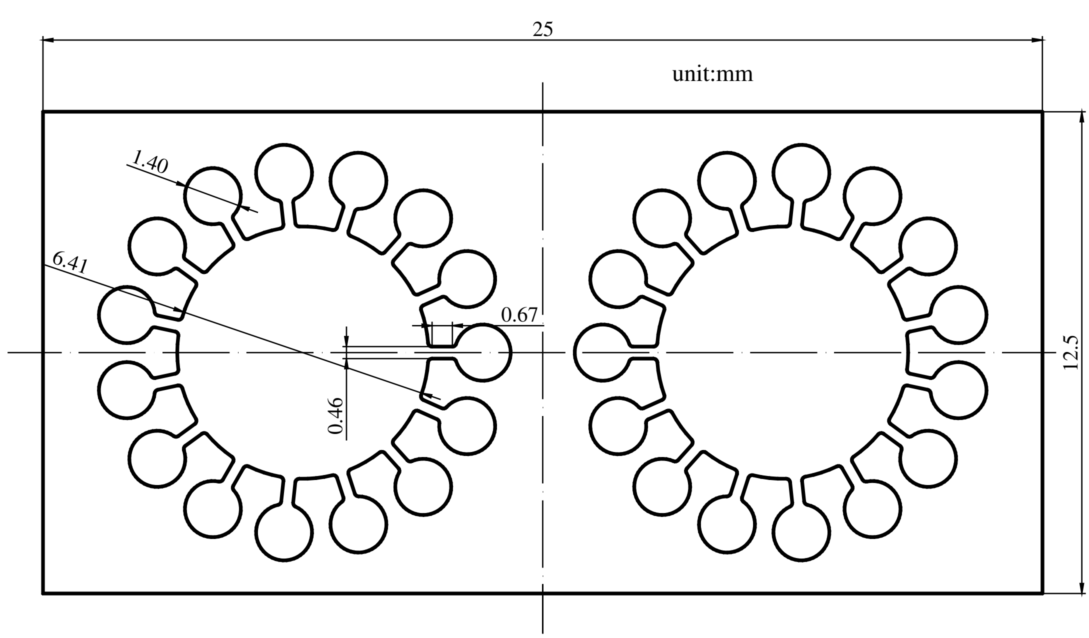

Fig. 11. Geometry of heat pipe (two cores) with axial "Ω"-shaped grooves for experiment (axial length: 1850 mm, L_e = 700 mm, L_a = 560 mm, L_c = 590 mm).

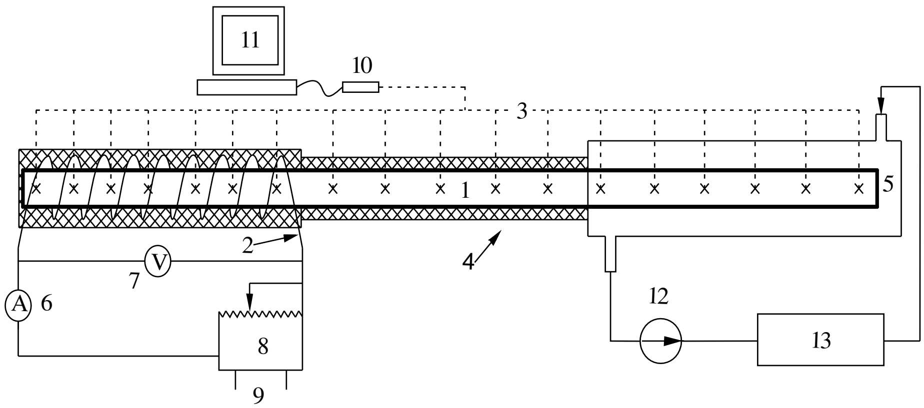

Fig. 12. Schematic of experimental set up. 1, Heat pipe; 2, electrical heater; 3, thermocouple; 4, thermal insulation; 5, tank; 6, amperemeter; 7, voltmeter; 8, voltage regulator; 9, power supply; 10, data acquisition; 11, computer; 12, pump; 13, constant temperature water bath.

Table 2
Comparison of experimental data with calculation results for single core

Working temperature T_{work} (K)	Maximum heat transport capability Q_{max} (W)		Error %
	Measurement	Calculation	
319.3	163	176	8.0
311.1	172	196	14.0
304.5	207	212	2.4

good agreement between the numerical results and the experimental data verifies the present model is reasonable.

5. Conclusions

A theoretical model of fluid flow and heat transfer in a heat pipe with axial "Ω"-shaped grooves is developed and solved numerically to obtain the heat pipe performance and maximum heat transport capability. The model includes the effects of the liquid–vapor interfacial shear stress, variation of meniscus radius and the contact angle. The effect of vapor core and wick structure on fluid flow characteristics, the effect of heat load on capillary radius at evaporator end cap, and the effect of wick size and working temperature on heat transfer performance are all analyzed and discussed. The axial distributions of capillary radius, fluid pressure and mean velocity are solved. And the accuracy of the model is also verified by the experiment. The conclusions can be summarized as:

(1) The shear force of the vapor on the liquid varies with the vapor channel geometry for a small contact angel while it is almost no variation with the geometry when θ is larger than 60°.
(2) The meniscus radius at the evaporator end cap depends upon the heat load for a given heat pipe. And when the minimal meniscus radius at this point is approached, the heat pipe reaches the maximum heat transport capability.
(3) The capillary radius increases non-linearly along the axial direction, at the evaporator section it would increase slowly, while it begins to increase drastically at the beginning of the condenser section.
(4) The pressure in liquid would increase along the axial direction, and the narrow slot of the "Ω"-shaped groove weakens the shear force of vapor on liquid, hence the condensate will be driven from the condenser back easily to the evaporator effectively by the capillary force. The liquid pressure variation along the axial is much larger than what in vapor phase.
(5) The calculated maximum heat transport capability by present model is lower than what from Chi's model, in which the interfacial shear stress is neglected.
(6) Smaller wick slot width might increase not only capillary pumping force but also friction loss. In addition, larger wick diameter would increase liquid flow permeability but decrease effective thermal conductivity of wick structure layer. Therefore, based on the mechanical manufacture capacity, optimization design of the "Ω"-shaped wick geometry for both flow and thermal considerations is very important for engineering application.

Acknowledgements

The authors gratefully acknowledge the supports provided by National Natural Science Foundation of China No. 50806012 and Fok Ying Tung Young Teacher Education Foundation No. 101055.

References

[1] S.K. Thomas, V.C. Damle, Fluid flow in axial reentrant grooves with application to heat pipes, J. Thermophys. Heat Transfer 19 (2005) 395–405.
[2] W. Harwell, W. Kaufman, L. Tower, Reentrant groove heat pipe, in: Proceedings of the 12th AIAA Thermophysics Conference, New York, 1977, pp. 131–147.
[3] L.L. Vasiliev, Heat pipe in modern heat exchangers, Appl. Thermal Eng. 25 (1) (2005) 1–19.
[4] L.L. Vasiliev, Micro and miniature heat pipes–electronic component coolers, Appl. Thermal Eng. 28 (4) (2008) 266–273.
[5] G. Manfred, S. Marcus, S. Valérie, C.Z. Mohamed, L. Monique, Thermal control of electronic equipment by heat pipes, Rev. Gén. Therm. 37 (5) (1998) 323–352.
[6] D.A. Benson, D.R. Adkins, G.P. Peterson, R.T. Mitchell, M.R. Tuck, D.W. Palmar, Turning silicon substrates into diamond: micromachining heat pipes, in: Advances in Design, Materials and Processes for Thermal Spreaders Heat Sinks Workshop, Vail, CO, 1996, pp. 19–21.
[7] D.A. Benson, R.T. Mitchell, M.R. Tuck, D.R. Adkins, D.W. Palmar, Micro-machined heat pipes in silicon MCM substrates, in: Proceeding IEEE Multichip Module Conference, Santa Clara, CA, 1996, pp. 127–129.
[8] D.A. Benson, R.T. Mitchell, M.R. Tuck, D.W. Palmar, G.P. Peterson, Ultrahigh-capacity micromachined heat spreaders, Microscale Thermophys. Eng. 2 (1998) 21–30.
[9] D.A. Benson, C.V. Robino, D.W. Palmar, Heat pipe with improved wick structures, US Patent No. 6056044, 2000.
[10] S. Kalahasti, Y.K. Joshi, Performance characterization of a novel flat plate micro heat pipe spreader, IEEE Trans. Comp. Packag. Tech. 25 (2002) 554–560.
[11] M. Dubois, B. Mullender, W. Supper, Space qualification of high capacity grooved heat pipes, Society of Automotive Engineers, SAE Paper, 972453, Warrendale, PA, 1997.
[12] B. Suman, A steady state model and maximum heat transport capacity of an electrohydrodynamically augmented micro-grooved heat pipe, Int. J. Heat Mass Transfer 49 (2006) 3957–3967.
[13] H.B. Ma, G.P. Peterson, X.J. Lu, The influence of vapor–liquid interaction on the liquid pressure drop in triangle microgrooves, Int. J. Heat Mass Transfer 37 (1994) 2211–2219.

[14] S.W. Chen, J.C. Hsieh, C.T. Chou, H.H. Lin, S.C. Shen, M.J. Tsai, Experimental investigation and visualization on capillary and boiling limits of micro-grooves made by different processes, Sensors Actuators A Phys. 139 (2007) 78–87.

[15] D. Khrustalev, A. Faghri, Coupled liquid and vapor flow in miniature passages with microgrooves, J. Heat Transfer 121 (1999) 729–733.

[16] S.K. Thomas, R.C. Lykin, K.L. Yerkes, Full developed laminar flow in trapezoidal grooves with shear stress at the liquid–vapor interface, Int. J. Heat Mass Transfer 44 (2001) 3397–3412.

[17] S.J. Kim, J.K. Seo, K.H. Do, Analytical and experimental investigation on the operational characteristics and the thermal optimization of a miniature heat pipe with a grooved wick structure, Int. J. Heat Mass Transfer 46 (2003) 2051–2063.

[18] J.S. Suh, S.P. Young, Analysis of thermal performance in a micro flat heat pipe with axially trapezoidal groove, Tamkang, J. Sci. Eng. 6 (4) (2003) 201–206.

[19] E.M. Sparrow, A. Haji-Sheikh, Flow and heat transfer in ducts of arbitrary shape with arbitrary thermal boundary conditions, J. Heat Transfer 88C (1966) 351–358.

[20] F. White, Viscous Fluid Flow, McGraw-Hill, New York, 1991.

[21] J.P. Longtin, B. Badran, F.M. Gerner, A one-dimensional model of a micro heat pipe during steady-state operation, J. Heat Transfer 114 (1994) 709–715.

[22] B.R. Fang, J.D. Zhou, Y.M. Li, Matrix Theory (in Chinese), Tsinghua University Press, Beijing, 2004.

[23] A. Faghri, Heat Pipe Science and Technology, Taylor & Francis, Washington, DC, 1995.

[24] D. Khrustalev, A. Faghri, Thermal analysis of micro heat pipe, J. Heat Transfer 116 (1994) 189–198.

[25] D. Khrustalev, A. Faghri, Thermal characteristics of conventional and flat miniature axially grooved heat pipe, J. Heat Transfer 117 (1995) 1048–1054.

[26] R. Hopkins, A. Faghri, D. Khrustalev, Flat miniature heat pipes with micro capillary grooves, J. Heat Transfer 121 (1999) 102–109.

[27] S.W. Chi, Heat Pipe Theory and Practice, McGraw-Hill, New York, 1976.

[28] G.D. Wang, P. Cheng, H.Y. Wu, Unstable and stable flow boiling in parallel microchannels and in a single microchannel, Int. J. Heat Mass Transfer 50 (2007) 4297–4310.

[29] H.Y. Wu, P. Cheng, Boiling instability in parallel silicon microchannels at different heat flux, Int. J. Heat Mass Transfer 47 (2004) 3631–3641.

[30] R. Mosdorf, P. Cheng, H.Y. Wu, M. Shoji, Non-linear analyses of flow boiling in microchannels, Int. J. Heat Mass Transfer 48 (2005) 4667–4683.

[31] H.Y. Wu, P. Cheng, Visualization and measurements of periodic boiling in silicon microchannels, Int. J. Heat Mass Transfer 46 (2003) 2603–2614.